JOURNAL OF THERMOPHYSICS AND HEAT TRANSFER
Vol. 16, No. 3, July–September 2002

Use of Blackbody Optical Fiber Thermometers in High-Temperature Environments

Matthew R. Jones* and David G. Barker†
Brigham Young University, Provo, Utah 84602-4201

A blackbody optical fiber thermometer consists of an optical fiber whose sensing tip is given a metallic coating. The sensing tip of the fiber forms an isothermal cavity, and the emission from this cavity is approximately equal to the emission from a blackbody. Temperature readings are obtained by measuring the spectral intensity at the end of the fiber at two wavelengths. The ratio of these measurements is used to infer the temperature at the sensing tip. However, readings from blackbody optical fiber thermometers are corrupted by self-emission when extended portions of the fiber are exposed to elevated temperatures. Two possible methods are described for correcting the problem caused by self-emission by the fiber. The first method is two-fiber optical fiber thermometry. In this method a second fiber is positioned parallel to the original fiber. The fibers are identical except that the second fiber has a reflecting coating instead of a blackbody cavity at its tip. Because both the emitting and reflecting fibers are exposed to the same thermal environment, measurements of the intensity at the end of the reflecting fiber can be used to eliminate error caused by emission by the fiber. The second approach is spectral remote sensing. In this method the intensity exiting the fiber is measured in portions of the visible and infrared spectrum. The measured spectral intensities are used to reconstruct the temperature profile along the fiber.

Nomenclature

A	=	amplitude of a perturbation
c_0, c_1, c_2	=	radiation constants
E	=	radiative flux
f	=	fitness function
I	=	intensity
I_b	=	blackbody intensity
K_a	=	spectral absorption coefficient for the optical fiber
k	=	imaginary part of refractive index for Al_2O_3
L	=	length of the optical fiber
M	=	measurement
N_p	=	number of points in the temperature profile
N_λ	=	number of wavelengths
n	=	real part of refractive index for Al_2O_3
s	=	smoothness criterion
$T(t)$	=	temperature profile
T_{bf}	=	measured tip temperature obtained using the standard method
T_{rs}	=	measured tip temperature obtained using the remote sensing method
T_0	=	true temperature of the sensing tip
T_{2f}	=	measured tip temperature obtained using the two-fiber method
t	=	optical length of the fiber
z	=	distance along the axis of the fiber
β	=	fiber constant
γ	=	calibration factor
$\Delta\Omega$	=	solid angle defined by the numerical aperture of the fiber
ε	=	normalized rms error in the calculated radiative fluxes
ε_{avg}	=	average of the normalized rms errors for the current generation
$\varepsilon_{\max}$	=	maximum normalized rms error for the current generation
$\varepsilon_{\min}$	=	minimum normalized rms error for the current generation
ρ	=	reflectivity of the reflective coating

Subscripts

e	=	emitting
i, j, k	=	indices
r	=	reflecting
λ	=	wavelength
ν	=	frequency

Received 20 August 2001; revision received 21 September 2001; accepted for publication 11 March 2002.

*Assistant Professor, Department of Mechanical Engineering, 435 Crabtree Technology Building, P.O. Box 24201.

†Research Assistant, Department of Mechanical Engineering, 435 Crabtree Technology Building, P.O. Box 24201.

Introduction

OPTICAL fiber thermometers (OFT) are devices that use photonic signals to sense temperatures. Compared to other temperature sensors, OFT have the following advantages: long-term stability, immunity to electromagnetic interference, high sensitivity, and the capability of withstanding harsh environments.

Several types of OFT have been developed.[1] Interferometric sensors use the thermal expansion of an optical fiber to perturb a laser signal, and the temperature is inferred using interferometry. Fluoroptic sensors have a photoluminescent material attached to the active end of an optical fiber. An excitation pulse from a pulsed laser or flash lamp activates the sensing tip, and the temperature is inferred from the decay time of the photoluminescent signal. Blackbody sensors consist of a high-temperature optical fiber with an opaque cavity attached to the sensing tip. The spectral radiative flux detected at the end of the fiber is related to the temperature of the cavity via Planck's law.[2] Fluoroptic and interferometric sensors are very sensitive, but their temperature ranges are limited by material properties. Blackbody sensors can operate over a wide range of temperatures, and so blackbody sensors are generally used in high-temperature applications.

An example of an application in which the use of blackbody OFT is highly desirable is in the thermal control system of microgravity furnaces that will fly on the International Space Station. The design of these furnaces is similar to that of a Bridgman furnace and consists of a heater core, insulation jacket, instrumentation, coolant loop

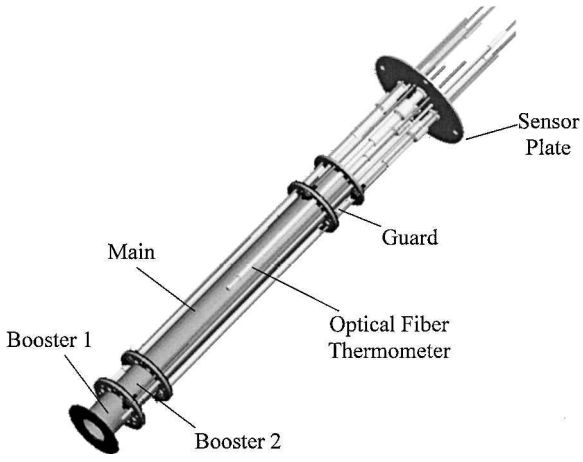

Fig. 1 Hot zone assembly for a microgravity furnace.

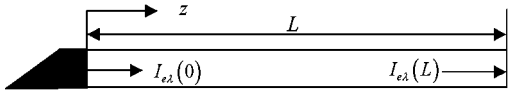

Fig. 2 Schematic diagram for a blackbody optical fiber thermometer. The sensing tip ($z = 0$) is coated with a thin metallic film to create a small isothermal cavity at a temperature of T_0. The spectral intensity emitted by the cavity $I_\lambda(0)$ is approximately equal to the spectral intensity emitted by a blackbody $I_{b\lambda}(T_0)$.

components, a cold zone for directional solidification, and a quench zone for rapid quenching. A sketch of a typical furnace's hot zone is shown in Fig. 1. The heater core is approximately 30 cm in length and contains four heated zones: Booster 1, Booster 2, Main, and Guard. The sensor plate is cooled in order to maintain sensors and other instrumentation at acceptable operating temperatures. The cold zone is a water-cooled chill block (not shown) that is located adjacent to Booster 1. This design produces the high thermal gradients required for directional solidification experiments.

As shown in Fig. 1, the OFT are aligned with the axis of the furnace in these preliminary designs, and an extended portion of the fiber is exposed to elevated temperatures. Jones et al.[3] showed that emission from portions of the fiber other than the sensing tip corrupt the temperature measurements under these conditions.

This paper describes two possible methods for correcting the problem caused by self-emission by the fiber. The first method is two-fiber optical fiber thermometry.[4] In this method a second fiber is positioned parallel to the original fiber. The fibers are identical except that the second fiber has a reflective layer at its tip instead of a blackbody cavity. Because both the emitting and reflecting fibers are exposed to the same thermal environment, measurements of the intensity at the end of the reflecting fiber can be used to eliminate error caused by emission by the fiber. The second approach is motivated by previous studies in which spectral remote sensing was used to determine the temperature profiles in semitransparent solids and high-temperature gases.[5–8] In this method the intensity exiting the fiber is measured in portions of the visible and infrared spectrum. The measured spectral intensities are used to reconstruct the temperature profile along the fiber.

Blackbody Optical Fiber Thermometry

A typical blackbody OFT is illustrated in Fig. 2 (Ref. 2). The probe consists of a sapphire (Al_2O_3) fiber whose sensing tip is given a metallic coating. The sensing tip of the fiber forms an isothermal cavity, so that emission from this cavity is approximately equal to the emission from a blackbody. The spectral radiative flux incident on the detector is equal to the product of the spectral intensity and the solid angle subtended by the detector. The ratio of the spectral radiative flux incident on the detector and the output of the detector defines the calibration factor γ_λ:

$$I_{e\lambda}(t_{\lambda L})\Delta\Omega = E_{e\lambda} = \gamma_\lambda M_{e\lambda} \tag{1}$$

An equation relating the spectral intensity at the end of the fiber to the spectral intensity emitted from the cavity is needed to infer the temperature at the sensing tip. The required relationship is obtained by modeling the fiber as an absorbing, emitting, and nonscattering medium. Because the radiation is transmitted through air or a vacuum after leaving the fiber, it is convenient to use frequency as the spectral variable. The spectral intensity at each point along the fiber is given by the solution of Eq. (2) with the boundary condition specified by Eq. (3)[9]:

$$\frac{dI_{ev}}{dz} = -K_{av}I_{ev} + K_{av}I_{bv}[T(z)] \tag{2}$$

$$I_{ev}(0) = I_{bv}(T_0) \tag{3}$$

Solving for $I_{bv}(T_0)$ gives

$$I_{bv}(T_0) = I_{ev}(T_{vL})\exp\{t_{vL}\} - \int_0^{t_{vL}} I_{bv}[T(t_v)]\exp\{t_v\}\,dt_v \tag{4}$$

where $t_v = K_{av}z$ and $t_{vL} = K_{av}L$. The exponential in the first term on the right-hand side of Eq. (4) corrects for the attenuation caused by absorption of the intensity as it propagates along the fiber. The integral on the right-hand side of Eq. (4) represents noise caused by emission by the fiber. The usual procedure is to assume that this integral is negligible:

$$I_{bv}(T_0) \approx I_{bv}(T_{bf}) = I_{ev}(t_{vL})\exp\{t_{vL}\} \tag{5}$$

Note that the estimate of the spectral blackbody intensity given by Eq. (4) is greater than the true value, so that the measured temperature T_{bf} will be greater than the actual temperature T_0.

For the temperatures and the wavelengths of interest, Wien's limit can be used to approximate the spectral intensity of a blackbody:

$$I_{bv}(T_{bf}) = \frac{2h\nu^3 n_\nu^2}{c_0^2[\exp\{h\nu/kT_{bf}\} - 1]} \approx \frac{2h\nu^3 n_\nu^2}{c_0^2\exp\{h\nu/kT_{bf}\}} \tag{6}$$

The spectral radiative flux leaving the fiber is measured by a spectrometer as a function of wavelength. Therefore, it is convenient at this point to convert the spectral variable from frequency to wavelength. Because the radiation leaves the fiber and propagates through air or a vacuum before being detected, the appropriate conversion formula is[9]

$$I_{b\lambda}(T_{bf}) = \left(c_0/\lambda^2\right)I_{bv}(T_{bf}) \tag{7}$$

Combining Eq. (1) with Eqs. (5–7) gives an expression for the dimensionless emission:

$$\exp\{-c_2/\lambda T_{bf}\} = \lambda^5\beta_\lambda M_{e\lambda} \tag{8}$$

where β_λ is a grouping of physical constants and parameters related to the properties and dimensions of the optical fiber. In practice the fiber constant will be determined as part of the calibration procedure:

$$\beta_\lambda = \frac{\pi\gamma_\lambda\exp\{t_{\lambda L}\}}{c_1 n_\lambda^2\Delta\Omega} \tag{9}$$

The temperature is obtained by making measurements at two wavelengths, λ_1 and λ_2. Using Eq. (8), the ratio of $M_{e\lambda_1}$ to $M_{e\lambda_2}$ is

$$\frac{M_{e\lambda_1}}{M_{e\lambda_2}} = \frac{\lambda_2^5\beta_{\lambda_2}\exp\{c_2/\lambda_2 T_{bf}\}}{\lambda_1^5\beta_{\lambda_1}\exp\{c_2/\lambda_1 T_{bf}\}} \tag{10}$$

The measured temperature is obtained by solving for T_{bf}:

$$T_{bf} = \frac{c_2(1/\lambda_2 - 1/\lambda_1)}{\ell n\left[\lambda_1^5\beta_{\lambda 1}M_{e\lambda_1}/\lambda_2^5\beta_{\lambda 2}M_{e\lambda_2}\right]} \tag{11}$$

Recall that the integral in Eq. (4) represents the portion of the detected radiative flux that is caused by emission from the fiber. This integral is negligible when the temperature of the fiber is low $\{I_{b\lambda}[T(t_\lambda)] \approx 0$ for $t_\lambda \neq 0\}$ or the optical depth of the fiber is small ($t_{\lambda L} \approx 0$). However, Jones et al.[3] showed that when blackbody OFT are place in a high-temperature environment such as that illustrated in Fig. 1 the emission by the fiber is significant, and neglecting the integral in Eq. (4) can lead to unacceptable errors. This paper focuses on two methods of accounting for the effects from emission by the fiber. The first approach is two-fiber optical fiber thermometry, and the second approach is spectral remote sensing.

Two-Fiber Optical Fiber Thermometry

One possible method of accounting for the integral in Eq. (4) is to position a second fiber next to the original fiber as illustrated in Fig. 3. The fibers are identical except that the second fiber has a reflective layer instead of a blackbody cavity at its tip. The first fiber is referred to as the emitting fiber, and the second fiber is referred to as the reflecting fiber. Because both the emitting and reflecting fibers are exposed to the same thermal environment, measurements of the spectral intensity at the end of the reflecting fiber can be used to eliminate error from emission by the fiber. Three possible methods of using the data from the reflecting fiber to correct the temperature measurements have been developed.[4] The most successful method is described next.

The governing equation and boundary condition for the spectral intensity propagating along the reflecting fiber are given by Eqs. (12) and (13):

$$\frac{dI_{r\nu}}{dz} = -K_{a\nu} I_{r\nu} + K_{a\nu} I_{b\nu}[T(z)] \tag{12}$$

$$I_{r\nu}(0) = \rho_\nu I^-_{r\nu}(L) + (1-\rho_\nu) I_{b\nu}(T_0) \tag{13}$$

Reflecting fibers can be fabricated by masking all but the tip of the fiber and sputtering a layer of MgO onto the fiber. The normal spectral reflectance of MgO is approximately 0.97 in the 0.4–1-μm spectral region.[10] The solution of Eqs. (12) and (13) gives

$$\exp\{t_{\nu L}\} I_{r\nu}(t_{\nu L}) = \rho_\nu I^-_{r\nu}(t_{\nu L}) \exp\{t_{\nu L}\} + (1-\rho_\nu) I_{b\nu}(T_0) + \int_0^{t_{\nu L}} \exp\{t_\nu\} I_{b\nu}[T(t_\nu)]\, dt_\nu \tag{14}$$

An expression for $I^-_{r\nu}(t_{\nu L})$ is obtained by solving for the spectral intensity propagating along the reflecting fiber in the direction of the reflecting tip. The appropriate equation and boundary condition are

$$\frac{dI^-_{r\nu}}{d\zeta} = -K_{a\nu} I^-_{r\nu} + K_{a\nu} I_{b\nu}[T(\zeta)] \tag{15}$$

$$I^-_{r\nu}(0) = 0 \tag{16}$$

The boundary condition given by Eq. (16) is appropriate because the end of the fiber connected to the detection system is maintained at a low temperature. Therefore, emission at the wavelengths of interest is negligible. Solving Eqs. (15) and (16) gives

$$I^-_{r\nu}(t_{\nu L}) = \int_0^{t_{\nu L}} \exp\{-t_\nu\} I_{b\nu}[T(t_{\nu L} - t_\nu)]\, dt_\nu \tag{17}$$

Substituting Eq. (17) into Eq. (14) gives

$$(1-\rho_\nu) I_{b\nu}(T_0) = \exp\{t_{\nu L}\} I_{r\nu}(t_{\nu L}) - \int_0^{t_{\nu L}} \{\rho_\nu \exp\{-t_\nu\} I_{b\nu}[T(t_{\nu L} - t_\nu)] + \exp\{t_\nu\} I_{b\nu}[T(t_\nu)]\}\, dt_\nu \tag{18}$$

Substituting Eq. (4) into Eq. (18) gives

$$\exp\{t_{\nu L}\}[(1-\rho_\nu) I_{e\nu}(t_{\nu L}) - I_{r\nu}(t_{\nu L})] = -\rho_\nu \int_0^{t_{\nu L}} \{\exp\{t_\nu\} I_{b\nu}[T(t_\nu)] + \exp\{-t_\nu\} I_{b\nu}[T(t_{\nu L} - t_\nu)]\}\, dt_\nu \tag{19}$$

An average temperature is defined such that

$$I_{b\nu}(T_a) = \frac{1}{e^{t_{\nu L}} - e^{-t_{\nu L}}} \int_0^{t_{\nu L}} \{\exp\{t_\nu\} I_{b\nu}[T(t_\nu)] + \exp\{-t_\nu\} I_{b\nu}[T(t_{\nu L} - t_\nu)]\}\, dt_\lambda \tag{20}$$

The combination of Eqs. (19) and (20) gives

$$I_{b\nu}(T_a) = \frac{\exp\{t_{\nu L}\}[I_{r\nu}(t_{\nu L}) - (1-\rho_\nu) I_{e\nu}(t_{\nu L})]}{\rho_\nu(\exp\{t_{\nu L}\} - \exp\{-t_{\nu L}\})} \tag{21}$$

The average temperature is used to approximate the integral in Eq. (4). That is, it is assumed that

$$I_{b\nu}(T_0) \approx I_{b\nu}(T_{2f}) = I_{e\nu}(t_{\nu L}) \exp\{t_{\nu L}\} - I_{b\nu}(T_a) \int_0^{t_{\nu L}} \exp\{t_\nu\}\, dt_\nu \tag{22}$$

Substituting Eq. (21) into Eq. (22) gives

$$I_{b\nu}(T_{2f}) = \frac{\exp\{t_{\nu L}\}}{\exp\{t_{\nu L}\} - \exp\{-t_{\nu L}\}} \times \left(1 - \exp\{-t_{\nu L}\} + \frac{\exp\{t_{\nu L}\} - 1}{\rho_\nu}\right) I_{e\nu}(t_{\nu L}) - \frac{\exp\{t_{\nu L}\}}{\exp\{t_{\nu L}\} - \exp\{-t_{\nu L}\}} \left(\frac{\exp\{t_{\nu L}\} - 1}{\rho_\nu}\right) I_{r\nu}(t_{\nu L}) \tag{23}$$

Similar to Eq. (1), the relationship between the spectral intensity at the end of the reflecting fiber and the measured value is

$$I_{r\lambda}(t_{\lambda L}) \Delta\Omega = \gamma_\lambda M_{r\lambda} \tag{24}$$

Again, an approximate temperature is obtained by making measurements at two wavelengths, λ_1 and λ_2. Following the same steps used to obtain Eq. (11) results in

$$T_{2f} = c_2 \left(\frac{1}{\lambda_2} - \frac{1}{\lambda_1}\right) \Bigg/ \ell n \left(\frac{\sinh(t_{\lambda_2 L})}{\sinh(t_{\lambda_1 L})} \left\{ \frac{\left[1 - e^{-t_{\lambda_1 L}} + (e^{t_{\lambda_1 L}} - 1)/\rho_{\lambda_1}\right] \lambda_1^5 \beta_{e\lambda_1} M_{e\lambda_1} - \left[(e^{t_{\lambda_1 L}} - 1)/\rho_{\lambda_1}\right] \lambda_1^5 \beta_{r\lambda_1} M_{r\lambda_1}}{\left[1 - e^{-t_{\lambda_2 L}} + (e^{t_{\lambda_2 L}} - 1)/\rho_{\lambda_2}\right] \lambda_1^5 \beta_{e\lambda_2} M_{e\lambda_2} - \left[(e^{t_{\lambda_2 L}} - 1)/\rho_{\lambda_2}\right] \lambda_1^5 \beta_{r\lambda_2} M_{r\lambda_2}} \right\} \right) \tag{25}$$

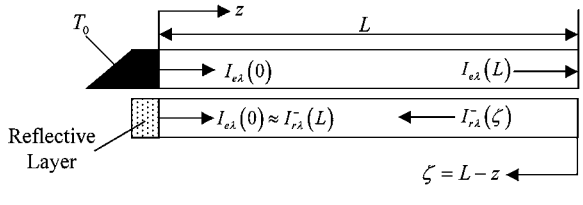

Fig. 3 Schematic diagram for a two-fiber optical fiber thermometer.

Spectral Remote Sensing

In this method the dimensionless emission exiting the fiber is measured throughout portions of the visible and infrared spectrums. The measurements are used to reconstruct the temperature profile along the length of the fiber. Based on Eq. (4), the temperature profile is related to the dimensionless emission through an integral equation.

$$\lambda_i^5 \beta_{\lambda_i} M_{e\lambda_i} = \frac{1}{\exp\{c_2/\lambda_i T_0\} - 1} + \int_0^{t_{\lambda_i L}} \frac{\exp\{t_{\lambda_i}\}}{\exp\{c_2/\lambda_i T(t_{\lambda_i})\} - 1} \, dt_\lambda \tag{26}$$

An estimate of the temperature profile is obtained by inverting Eq. (26). This equation is classified as a Fredholm integral equation of the first kind. This type of equation is frequently encountered in the solution of inverse problems involving radiative transfer,[11] and it is known that the solution to an equation of this type is not unique. Consideration of the integral of a sinusoidal function with an arbitrarily large amplitude shows that Eq. (26) allows multiple solutions. According to the Riemann–Lebesgue lemma,[12]

$$\lim_{\omega \to \infty} \int_0^{t_{\lambda_i L}} A \sin(\omega t_{\lambda_i}) \, dt_{\lambda_i} = 0 \tag{27}$$

Therefore,

$$\int_0^{t_{\lambda L}} \frac{\exp\{t_{\lambda_i}\}}{\exp\{c_2/\lambda_i T(t_{\lambda_i})\} - 1} \, dt_\lambda = \lim_{\omega \to \infty} \int_0^{t_{\lambda_i L}} \left[\frac{\exp\{t_{\lambda_i}\}}{\exp\{c_2/\lambda_i T(t_{\lambda_i})\} - 1} + A \sin(\omega t_{\lambda_i}) \right] dt_{\lambda_i} \tag{28}$$

Equation (28) shows that for arbitrarily large perturbations A there is a frequency such that

$$\frac{\exp\{t_{\lambda_i}\}}{\exp\{c_2/\lambda_i T(t_{\lambda_i})\} - 1} + A \sin(\omega t_{\lambda_i})$$

will satisfy Eq. (26). Thus, it is clear that an infinite number of temperature profiles will satisfy Eq. (26). However, the spurious temperature profiles will exhibit high-frequency oscillations that allow them to be rejected based on physical considerations. In the present case it is reasonable to require that the temperature profile be smooth and nonnegative.

Because there is not a unique solution, conventional gradient-based search methods are likely to become trapped in local minima and are generally ineffective in finding the solution in cases such as this. A directed random search method such as a genetic algorithm is capable of finding the global optimal solution in complex, multi-dimensional search spaces. Genetic algorithms are based on the principle of natural selection or survival of the fittest. The structure of a typical genetic algorithm is shown in Fig. 4. The following paragraphs briefly describe the aspects of the implementation unique to this study. Detailed discussions of the fundamentals of genetic algorithms and descriptions of the wide variety of optimization problems successfully treated using genetic algorithms are available in the literature.[13,14]

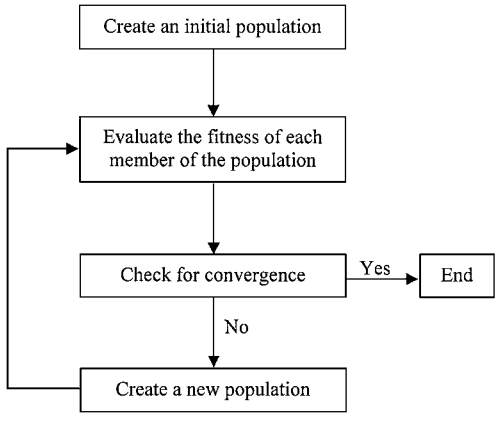

Fig. 4 Flowchart for a simple genetic algorithm.

Selection of an Initial Population

An initial population of 100 possible temperature profiles was created by randomly perturbing an initial estimate of the temperature profile along the optical fiber.

Fitness Function

The error for the jth possible temperature profile in the population is the rms value of difference between the measurements and the value of $(\lambda_i^5 \beta_{\lambda_i} M_{\lambda_i})_j$ obtained from Eq. (26) using the jth temperature profile:

$$\varepsilon_j = \frac{1}{N_\lambda} \sum_{i=1}^{N_\lambda} \sqrt{\left(\frac{\left(\lambda_i^5 \beta_{\lambda_i} M_{\lambda_i}\right)_{\text{measured}} - \left(\lambda_i^5 \beta_{\lambda_i} M_{\lambda_i}\right)_j}{\left(\lambda_i^5 \beta_{\lambda_i} M_{\lambda_i}\right)_{\text{measured}}} \right)^2} \tag{29}$$

The smoothness of each temperature profile was quantified using the second finite differences:

$$s_j = \frac{2}{N_p - 2} \sum_{k=2}^{N_p - 1} \sqrt{\left\{ \frac{[T(z_{k+1}) - T(z_k)](z_k - z_{k-1}) - [T(z_k) - T(z_{k-1})](z_{k+1} - z_k)}{(z_{k+1} - z_{k-1})(z_{k+1} - z_k)(z_k - z_{k-1})} \right\}^2} \tag{30}$$

The fitness of the jth possible temperature profile was defined as

$$f_j = \frac{\varepsilon_{\max} - \varepsilon_j}{\varepsilon_{\text{avg}}} + \frac{s_{\max} - s_j}{s_{\text{avg}}} \tag{31}$$

where $\varepsilon_{\max}$ and ε_{avg} are the maximum and average values for the current generation and $s_{\max}$ and s_{avg} are the maximum and average values of the smoothness criterion for the current generation.

Creation of a New Population

The possible temperature profile with the greatest fitness value and the possible temperature profile with the minimum error from the previous generation were copied directly into the new generation. The next 20 possible temperature profiles in the new population were created by repeatedly applying a smoothing operator to the possible temperature profile with the minimum error. Ten of the 20 new possible temperature profiles were created using the average of the temperature at a point with its two nearest neighbors. The next 10 new possible temperature profiles were created using the average of the temperature at a point with its four nearest neighbors. The remaining 78 possible temperature profiles in the new generation were created using the crossover and mutation operators.[13,14] The crossover operation consists of selecting two possible temperature profiles according to their fitness values. A crossover site for each point in the temperature profile was randomly selected, and the portion of the temperature profile above the crossover site in the first possible profile was combined with the remaining portion of the second possible profile to create a new possible temperature profile. The mutation operator was applied after the new generation had been filled. The mutation operator consists of randomly selecting 1% of all of the temperature values and then randomly perturbing these values within a range of ±400 K.

The process of selection, crossover, and mutation continued until the following criteria were met. First, the profile with the lowest rms error for the current generation had to reach a specified minimum at the same time the average of the rms errors for the entire population reached a specified value. If these two criteria were satisfied and

the maximum actual error of the radiant flux compared to the measured flux was less than a specified tolerance, the algorithm would terminate and yield the most-fit solution. The algorithm was also terminated if significant improvement were not made over 12 generations for cases 1 and 2 and over 14 generations for case 3. This was determined by the variation of the rms average error; if it did not change more than a specified amount over 12 generations, the algorithm was terminated, and the results returned (see Figs. 5–7 for the criteria values for each case).

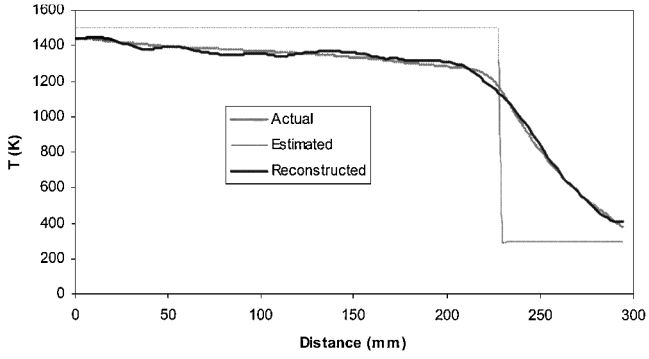

Fig. 5 Reconstructed temperature profile for case 1. Convergence criteria: $\varepsilon_{min} = 0.001$, $\varepsilon_{ave} = 0.015$, maximum radiant flux error = 1.8%, maximum generations = 500, tolerance for equivalent generations = 0.001, consecutive equivalent generations = 12; 185 generations were required to converge.

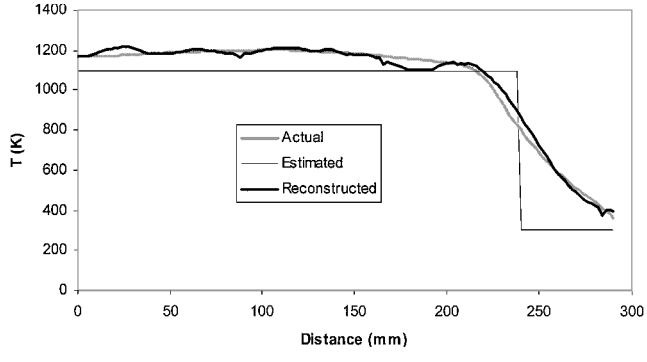

Fig. 6 Reconstructed temperature profile for case 2. Convergence criteria: $\varepsilon_{min} = 0.003$, $\varepsilon_{ave} = 0.06$, maximum radiant flux error = 1.8%, maximum generations = 500, tolerance for equivalent generations = 0.001, consecutive equivalent generations = 12; 185 generations were required to converge.

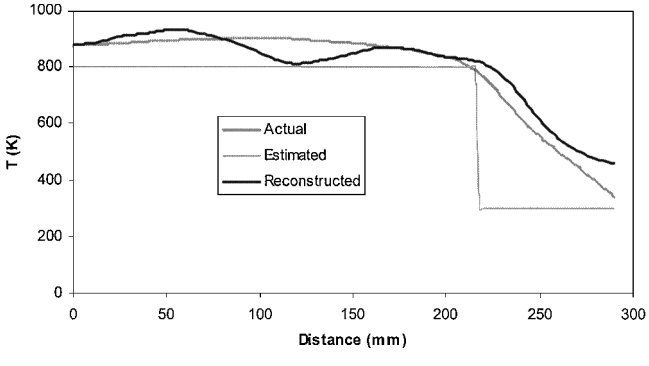

Fig. 7 Reconstructed temperature profile for case 3. Convergence criteria: $\varepsilon_{min} = 0.005$, $\varepsilon_{ave} = 0.35$, maximum radiant flux error = 1.8%, maximum generations = 1500, tolerance for equivalent generations = 0.004, consecutive equivalent generations = 14; 589 generations were required to converge.

Simulated Temperature Measurements

Three typical axial temperature profiles for the microgravity furnace illustrated in Fig. 1 were obtained from a detailed thermal model (*Thermal Design Data Book, Quench Module Insert, Preliminary Design Review*, NASA, Tec-Masters, Inc., and Sverdrup Technologies, 1999, personal communication). Simulated measurements of the dimensionless emission were calculated using these temperature profiles and Eq. (26) for a number of wavelengths. Values for the spectral absorption coefficients were calculated using Eq. (32) and linear interpolation of tabular data available for the imaginary part of the refractive index for sapphire[9]:

$$K_{a\lambda} = 4\pi k/\lambda \tag{32}$$

Figure 8 shows the spectral absorption coefficient used in this study. Because the wavelength at which the peak emission occurs increases as the average temperature decreases, it would be preferable to make measurements at longer wavelengths to reconstruct temperature profiles with lower average temperatures. However, obtaining measurements at longer wavelengths is difficult because of increased absorption, and measurements at longer wavelengths lead to very large dimensionless emission measurements, $\lambda^5 \beta_{e\lambda} M_{e\lambda}$. The magnitude of the measurements at these wavelengths would weight the lower temperature portion of the temperature profile too heavily. For these reasons the maximum wavelength used in this study was 4.0 μm, and it is expected that the reconstruction of the temperature profile will be more difficult as the average temperature decreases.

For the remote sensing approach 51 wavelengths between 0.5 and 4.0 μm were used to reconstruct the temperature profiles in each of the three cases. The wavelengths used in the standard and in the two-fiber approaches were 0.8 and 0.95 μm. The measured tip temperature obtained using the standard approach is compared with the temperatures obtained using two-fiber OFT and the remote sensing approach in Table 1. Table 2 shows the average and maximum errors in the reconstructed temperature profiles for each of the three cases.

Table 1 Simulated tip temperature measurements

Case	T_0, K	T_{bf}, K	T_{2f}, K	T_{rs}, K
1	1440	1458	1440	1441
2	1169	1200	1169	1170
3	877	895	877	877

Table 2 Errors in the reconstructed temperature profiles

	High-temperature region		Low-temperature region	
Case	Average temperature error, %	Maximum temperature error, %	Average temperature error, %	Maximum temperature error, %
1	1.4	3.7	2.4	8.2
2	1.5	6.9	5.1	9.4
3	3.5	11.1	15.0	35.5

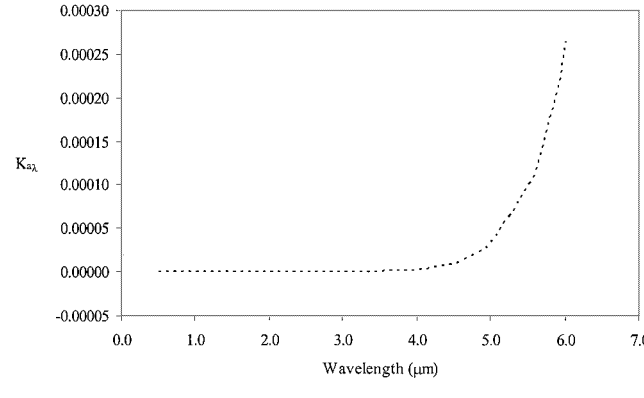

Fig. 8 Spectral absorption coefficient for Al_2O_3.

The errors in the measured temperatures obtained using the standard approach to blackbody OFT vary between 1 and 3%. The larger errors occur when portions of the fiber are at temperatures greater than the temperature of the sensing tip (cases 2 and 3). Note that, as predicted by comparing Eqs. (4) and (5), the measurements obtained using the standard approach are biased toward higher values.

The two-fiber approach eliminated the errors in all three cases. The tip temperature was also accurately measured (to within 0.15%) using the remote sensing approach in each of the three cases.

The reconstructed temperature profiles obtained using the remote sensing approach are compared with the actual temperature profiles in Figs. 5–7. The initial estimates used to obtain these results are also shown in these figures. As expected, the reconstructed temperature profile is more accurate when the profile has a higher average temperature. Table 2 lists the average and maximum deviations for the high- and low-temperature regions of the reconstructed temperature profiles for each case.

To asses the effect of the initial guess on the results, case 1 was run using the initial temperature profile shown in Fig. 9. After 466 generations the tip temperature had 0.14% error, and the entire profile had an average of 13.4% error. Comparison of these results with the results given in Fig. 5 and Table 2 shows that a poor initial guess greatly increases the time required to find a solution. However, this case and the results of other cases not presented indicate that the algorithm will eventually find a reasonably accurate solution independent of the choice made for the initial temperature profile.

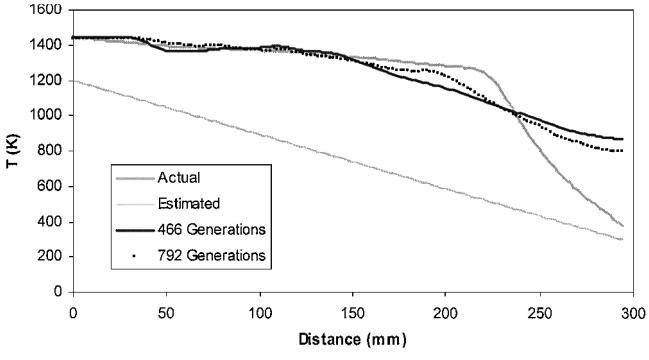

Fig. 9 Reconstructed profile for case 1 using a poor initial guess. After 466 generations the tip error is 0.14%, and the average error is 13.4%.

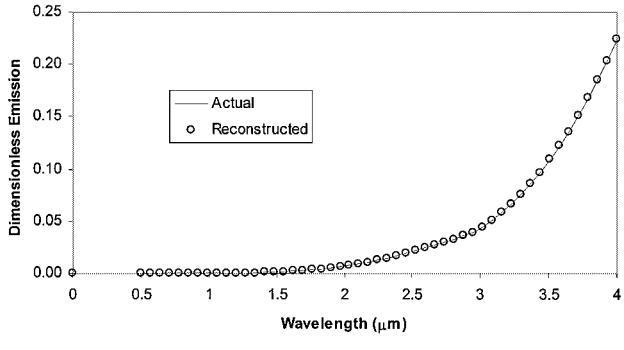

Fig. 10 Comparison of the dimensionless emission for the actual temperature profile and for the reconstructed profile for case 1.

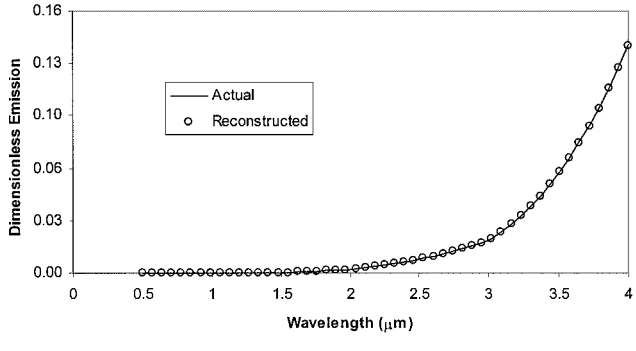

Fig. 11 Comparison of the dimensionless emission for the actual temperature profile and for the reconstructed profile for case 2.

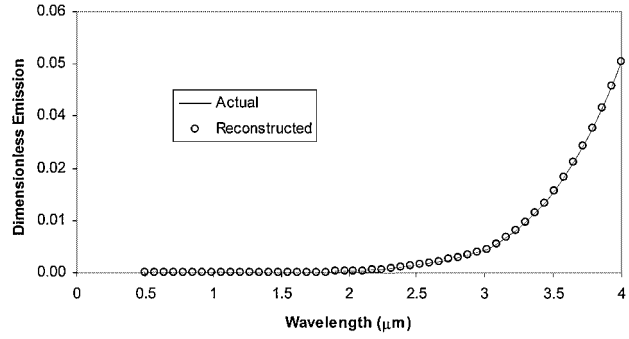

Fig. 12 Comparison of the dimensionless emission for the actual temperature profile and for the reconstructed profile for case 3.

Although the reconstructed temperature profiles differ from the actual temperature profile by as much as 20% in some locations, the dimensionless emission calculated using the actual temperature profile is in nearly perfect agreement with the dimensionless emission calculated using the reconstructed temperature profile. The dimensionless emission for the actual temperature profile and the reconstructed profile are plotted in Figs. 10–12. The maximum deviation for the three runs occurred in case 3, and it was 1.1% at 0.5 μm. The average deviation for this run was 0.49%.

Conclusions

The use of blackbody OFT offers a number of advantages, but errors caused by self-emission by the fiber prevent the use of the standard approach in applications where extended portions of the fiber are exposed to elevated temperatures. Two methods that eliminate the errors from emission by the fiber have been described in this paper.

The remote sensing method accurately retrieves the temperature at the tip of the OFT, eliminating the bias toward higher temperatures that occurs when the standard approach to blackbody OFT is employed. In addition, this approach produces an estimate of the temperature profile along the entire length of the fiber. The high-temperature portion of the reconstructed temperature profile agreed fairly well with actual temperature profile. As expected, the reconstructed temperature profiles were more accurate in the cases with higher averages temperatures.

Two-fiber OFT uses a second fiber with a reflecting tip to estimate the fraction of the measured spectral radiative flux that is from emission by the fiber. This approach also eliminates the bias toward higher temperatures and accurately measures the temperature at the tip of the OFT. The two-fiber approach is less complex than the remote sensing approach, and its use is preferable when the temperature profile along the length of the fiber is not of interest.

References

[1] Kreider, K. G., "Fiber-Optic Thermometry," *Applications of Radiation Thermometry*, edited by J. C. Richmond and D. P. DeWitt, American Society of Testing and Materials, Philadelphia, 1985, pp. 151–161.

[2] Dils, R. R., "High-Temperature Optical Fiber Thermometry," *Journal of Applied Physics*, Vol. 54, No. 3, 1983, pp. 1198–1201.

[3] Jones, M. R., Farmer, J. T., and Breeding, S. P., "Evaluation of the Use of Optical Fiber Thermometers for Thermal Control of the Quench Module Insert," *The 10th Thermal and Fluids Analysis Workshop* [CD-ROM], edited by A. Majumdar, NASA CP-2001-211141, 1999.

[4] Jones, M. R., Farmer, J. T., and Breeding, S. P., "Two-Fiber Optical Fiber Thermometry," *Proceedings of the ASME Heat Transfer Division*, HTD-Vol. 366-2, American Society of Mechanical Engineers, New York, 2000, pp. 139–146.

[5] Chupp, R. E., and Viskanta, R., "Development and Evaluation of a Remote Sensing Technique for Determining the Temperature Distribution in

Semitransparent Solids," *Journal of Heat Transfer*, Vol. 96, No. 3, 1974, pp. 391–397.

[6]Hommert, P. J., Viskanta, R., and Chupp, R. E., "Application of Spectral Remote-Sensing Method for Recovering Temperature Distribution in Glass," *Journal of the American Ceramic Society*, Vol. 58, No. 1–2, 1975, pp. 58–62.

[7]Hommert, P. J., and Viskanta, R., "High Temperature Gas Diagnostics by Spectral Remote Sensing," *International Journal of Heat and Mass Transfer*, Vol. 21, No. 6, 1978, pp. 769–781.

[8]Viskanta, R., Hommert, P. J., and Groninger, G. L., "Spectral Remote Sensing of Temperature Distribution in Semitransparent Solids Heated by an External Radiation Source," *Applied Optics*, Vol. 14, No. 2, 1975, pp. 428–437.

[9]Brewster, M. Q., *Thermal Radiative Transfer and Properties*, Wiley, New York, 1992, pp. 218–245.

[10]Touloukian, Y. S., and DeWitt, D. P. (eds.), *Thermal Radiative Properties: Nonmetallic Solids*, Vol. 8, Thermophysical Properties of Matter, Plenum, New York, 1972, pp. 299–312.

[11]Howell, J. R., Ezekoye, O. A., and Morales, J. C., "Inverse Design Model for Radiative Heat Transfer," *Journal of Heat Transfer*, Vol. 122, No. 3, 2000, pp. 492–502.

[12]Rudin, W., *Real and Complex Analysis*, McGraw–Hill, New York, 1966, pp. 109, 110.

[13]Goldberg, D. E., *Genetic Algorithms in Search, Optimization, and Machine Learning*, Addison Wesley Longman, Reading, MA, 1989.

[14]Pham, D. T., and Karaboga, D., *Intelligent Optimisation Techniques: Genetic Algorithms, Tabu Search, Simualted Annealing and Neural Networks*, Springer-Verlag, London, 2000.